Journal of Applied Physics

Non-destructive characterization of thin layer resonant tunneling diodes

Cite as: J. Appl. Phys. **126**, 124304 (2019); https://doi.org/10.1063/1.5113585
Submitted: 05 June 2019 . Accepted: 02 September 2019 . Published Online: 25 September 2019

Răzvan Baba, Kristof J. P. Jacobs, Brett A. Harrison, Ben J. Stevens, Toshikazu Mukai, and Richard A. Hogg

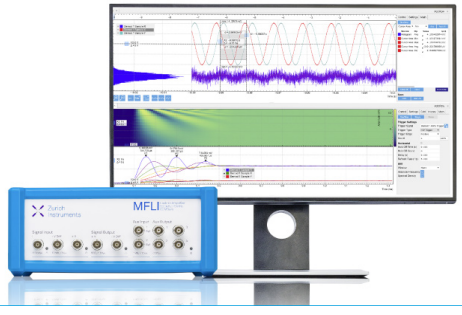

Journal of Applied Physics ARTICLE scitation.org/journal/jap

Non-destructive characterization of thin layer resonant tunneling diodes

Cite as: J. Appl. Phys. **126**, 124304 (2019); doi: 10.1063/1.5113585
Submitted: 5 June 2019 · Accepted: 2 September 2019 ·
Published Online: 25 September 2019

Răzvan Baba,[1,a)] Kristof J. P. Jacobs,[2] Brett A. Harrison,[2,3] Ben J. Stevens,[2,3] Toshikazu Mukai,[4] and Richard A. Hogg[1,b)]

AFFILIATIONS

[1]School of Engineering, University of Glasgow, Oakfield Avenue, G12 8LT Glasgow, United Kingdom
[2]Department of Electronic and Electrical Engineering, The University of Sheffield, Solly Street, S1 4DE Sheffield, United Kingdom
[3]EPSRC National Epitaxy Facility, North Campus, Broad Lane, S3 7HQ Sheffield, United Kingdom
[4]ROHM Co., Ltd., 21 Saiin Mizosaki-cho, Ukyo-ku, Kyoto 615-8585 Japan

Note: This paper is part of the Special Topic on Highly Mismatched Semiconductors Alloys: from Atoms to Devices.

[a)]elp13rb@gmail.com
[b)]richard.hogg@glasgow.ac.uk

ABSTRACT

We present an advanced nondestructive characterization scheme for high current density AlAs/InGaAs resonant tunneling diodes pseudomorphically grown on InP substrates. We show how low-temperature photoluminescence spectroscopy (LT-PL) and high-resolution X-ray diffractometry (HR-XRD) are complementary techniques to increase the confidence of the characterized structure. The lattice-matched InGaAs is characterized and found to be of high quality. We discuss the inclusion of an undoped "copy" well (C-well) in terms of enhancements to HR-XRD and LT-PL characterization and quantify the improved precision in determining the structure. As a consequence of this enhanced precision in the determination of physical structure, the AlAs barriers and quantum well (QW) system are found to contain nonideal material interfaces. Their roughness is characterized in terms of the full width to half-maximum of the split LT-PL emission peaks, revealing a ±1 atomic sheet variance to the QW width. We show how barrier asymmetry can be detected through fitting of both optical spectra and HR-XRD rocking curves.

I. INTRODUCTION

Resonant tunneling diodes (RTDs) are a class of unipolar, n+ doped shallow-emitter devices with active regions typically within 20–100 nm for electronic devices and typically 1 μm for optical devices. One of their salient features is a negative differential conductance region,[1] which has been exploited to realize some of the fastest oscillating solid state electronic devices available, demonstrated up to 1.98 THz[2] free space emission, with significant tuning ability.[3] The high-speed operation is made possible due to the weak confinement of the injected electrons between a double-barrier resonant tunneling structure (DBRTS). With adequately small device areas and barrier thickness within 2–4 pseudomorphically grown monolayers (1 ML = $a_{InP}/2 \approx 0.293$ nm) leading to current densities exceeding 10 mA μm^{-2}, the dwell time of the carriers inside the quantum well (QW) is expected to be within 10–100 fs.[4,5]

The resonance condition occurs when a given bias aligns the states of the injector level with the weakly bound state inside the DBRTS.[6] Therefore, the "difference" between the "weakly-confined QW energy level from the QW conduction band potential edge" [shown later in Fig. 5(a), inset] and "Fermi level at 0 V" is one of the critical parameters for the device operation: this energy difference correlates to the bias required to satisfy the resonance condition. In this work, this energy difference will be referred to as E_1, also referred to as the 1st quasibound state in the literature. We have previously modeled[7] the contribution of the E_1 state on the device operating characteristics, showing that it is an essential operational parameter that contributes to the efficiency of the device.

Given their impressive potential, RTDs are strong candidates for next-generation components in highly compact, high efficiency, monolithic, room temperature terahertz systems, with applications

ranging from high bandwidth line of sight atmospheric transceivers[8] to material identification and spectroscopy,[9] random number generation and quantum cryptography,[10] to high-speed mixed-mode circuits,[11] with further potential applications in security,[12] gas detection,[13] characterization of layered thin films, coatings, and paint,[14] astrophysics,[15] etc.

The design of RTDs varies with their intended application. For the case of optimizing terahertz emission power, we have shown that high current density is preferable to the peak-to-valley-current ratio.[7] This ratio is considered to be a marque of the quality of the epitaxial growth, as it is dependent on the full width to half-maximum (FWHM) of the E_1 state,[16] whereas high current densities are dependent on the doping scheme, barrier height and thickness, and contact quality. In order to create high quality metal-semiconductor interfaces, we have previously shown a dual-pass fabrication process,[17] obtaining peak current densities of 17 mA μm^{-2}. We have also shown that the AlAs/InGaAs/AlAs material system grown on InP is less thermally sensitive than previously thought, with an increase of valley current in the 15–300 K attributed to 29% due to heat alone.[18] The rest is given by the roughness of the heterointerfaces, resulting in increased carrier scattering.[19]

In this paper, we present an essential component toward improving the quality of the epitaxial interfaces, a nondestructive characterization scheme which can be used as a qualitative and quantitative measure to decrease the statistical process variability for the manufacturing of RTD material. To this end, the established complementary techniques of high-resolution X-ray diffractometry (HR-XRD) and low-temperature photoluminescence spectroscopy (LT-PL) are deployed in tandem. Firstly, we perform XRD modeling to analyze the sensitivity of the XRD method to structural layer changes. To facilitate the analysis, epitaxial "layer parameter linking" is performed, by grouping similar layer parameters to an expected growth rate. To further improve upon the XRD detectivity limit, we incorporate an electrically-neutral, buried copy of the active region (C-well). We then proceed to perform pump power-dependent low-temperature PL and fit the spectra to explain the individual contributions of the various electronic transitions. The fit spectra are solved using advanced modeling presented in the previous work,[7] converging to a number of possible solutions. Additionally, the linewidth and shape of the spectra provide detailed information about the AlAs/InGaAs interface quality. This enhanced determination of the physical structure is then fed back into the XRD fit to provide precise characterization of the epitaxy. Lastly, for confirmation purposes only, TEM dark-field microscopy is employed to obtain absolute information about the layer thickness to provide a baseline comparison (micrographs presented in Fig. 1).

In Fig. 1, we present the epitaxial layer structure used in this work. The bulk of the grown material is intentionally lattice-matched (LM) to the InP substrate, in order to minimize strain and misfit-induced defects. The ternary compound semiconductors $In_{0.53}Ga_{0.47}As$ and $Al_{0.48}In_{0.52}As$ are used to this effect. The DBRTS is strained pseudomorphically: structure A, as seen in Fig. 1, uses an overall tensile 4 ML symmetric AlAs barrier with a 13 ML QW, whereas structure B employs a 15 ML QW closer to the overall strain-balanced point. We have discussed these advanced structural design considerations of the DBRTS in the previous work.[7] The chemically sensitive dark-field (002) TEM images correspond to

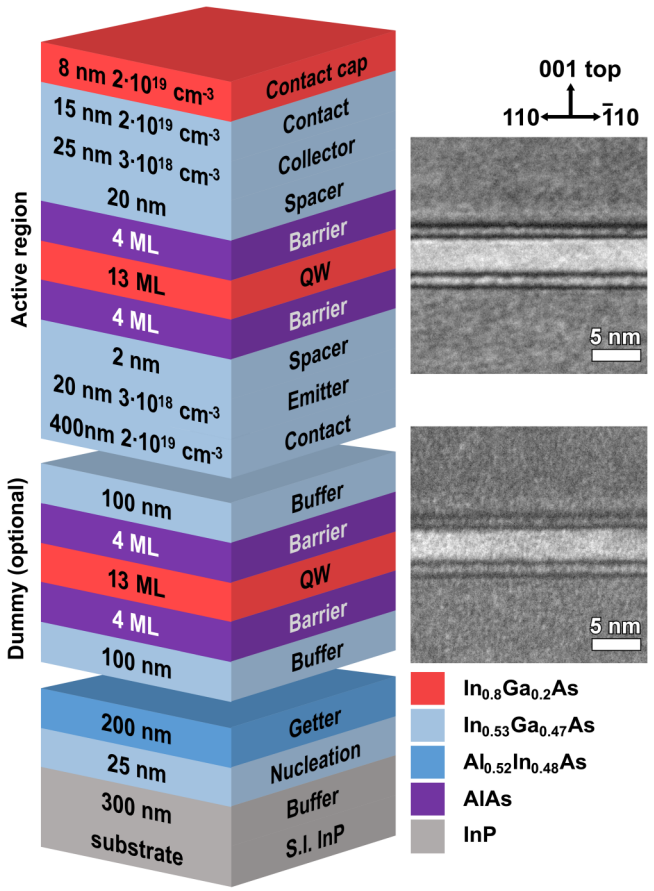

FIG. 1. Schematic (not to scale) of the epitaxial layer structure "A," with doping level (carriers cm^{-3}) and thickness (ML ~ 0.293 nm) (left side) and the role of the layer in the structure (right side). Material is color-coded, with the bulk grown material as lattice-matched InGaAs. The sides are dark-field (002) TEM images of the top and bottom double-barrier-QW structure, with the arrows referring to the crystal plane directions.

the two DBRTS regions (imaged after milling under an argon ion beam). The highly-strained QW has a different gray level compared to the thin AlAs and LM-InGaAs layers. The black region around the AlAs barriers appears due to a switch-over in the iii/v ratio affecting the (002) beam intensity.[20] An average across 1000 pixels reveals a top/QW/bottom barrier thickness of 1.134/3.885/1.341 nm and 1.066/3.919/1.238 nm for the top and bottom DBRTS, respectively. Despite the unintentional AlAs asymmetry, we note that the InGaAs-AlAs interface appears highly uniform. We attribute this asymmetry to gettering of atomic oxygen impurities present in the reactor chamber.

II. EXPERIMENTAL DESCRIPTION

The destructive TEM for structure A is used to confirm the findings in this section. In a high-volume industrial environment, it

may be desirable to eliminate or reduce reliance on routine costly characterization and sample preparation, particularly if this process has an associated failure rate: ultimate TEM resolution may only be achieved in a sample thinned to a few tens of nanometer.

The structures were grown on a Thomas Swan 7×2 in. robot-loaded close coupled showerhead MOVPE reactor using trimethylindium (TMI), trimethylgallium (TMG), and trimethylaluminium (TMA) as group 13 precursors, and arsine (AsH_3) and phosphine (PH_3) provide the source materials for group 15. Temperatures were measured through pyro-reflectance (Laytec EpiTT calibrated against a PT1000 probe) and material compositions with an Aixtron Epison 4 in-line gas concentration monitor. A 300 nm InP buffer was deposited at 560 °C on Fe doped InP (001) offcut by max. 0.1° toward (111). The subsequent layers were grown at 580 °C. 25 nm of InGaAs was grown straight after InP to improve the nucleation of AlInAs. The lattice-matched InGaAs layer composition was determined and calibrated against XRD, while the doping concentration was checked with electrochemical capacitance voltage[21] measurements and Hall Effect measurements. Structures A and B were grown in immediate succession to maintain reactor conditions and facilitate direct comparison.

The system performing XRD rocking curve in this paper is a Philips Analytical X'Pert PRO with a high-resolution PW3050/65 goniometer. A copper target radiation $K_{\alpha 2}/K_{\alpha 1}$ intensity ratio is −3 dB, lowered to −23 dB after conditioning, via a Ge-(220) 2-bounce asymmetric monochromator. This results in a negligible modeled contribution to the signal-to-noise ratio. The detector is a single point PW3011/20 proportion detector with a large window. Beam attenuation is provided by a graded Ni disk to avoid saturation. The HR-XRD ω–2θ (incident-scattering angles) (004) symmetric rocking curve is performed at cleanroom temperature (20 °C). The measurement integration time is 0.5 s/data point. The angle ψ is set to compensate for the substrate offcut, in this case optimized at 0.05°.

LT-PL experiments were performed at a fixed temperature of 15 K in a closed-cycle He cryostat. This temperature is chosen for reasons of convenience and ease of reproducibility. The excitation source is a 532 nm diode-pumped solid state laser, with an output optical power stability over 4 h of a measured ±1%. The laser is optically chopped within the 25 Hz bandwidth of the high gain Thorlabs PDF10C InGaAs fW receiver. A Bentham DMc150 double grating Czerny-Turner configuration monochromator with a peak responsivity at 1250 nm (gradually diverging to max. ±2 nm Railsback tuning curve error), dropping to ∼2% efficiency at 705 nm, with a further 650 nm cut-off dichroic mirror as a beam splitter in the system, and selectable long pass 700 and 1250 nm input filters. The slits were set to obtain a window resolution of ∼2 nm. The amplified signal is fed to a two-phase lock-in amplifier, synchronized with the optical chopper. Pump power-dependent micro-PL experiments were performed with excitation powers ranging 0.028–139 mW. The PL spectra are uncorrected for InGaAs and monochromator responsivity.

III. HIGH-RESOLUTION X-RAY DIFFRACTOMETRY

A. Sensitivity analysis

HR-XRD is a powerful technique for determining subnanometer feature sizes over a comparatively broad area. The spot size of a highly focused beam used in the analysis of semiconductor crystals is dependent upon the conditioning optics and may be typically expected to be within 0.1 and 2 mm, whereas the $CuK_{\alpha 1}$ emission is 0.15 nm. Therefore, in a single spot, there is a potential for a high amount of averaging of the diffracted electron counts. This poses a challenge, as high-level disorder crystals may not be characterized accurately, and low-resolution instruments will fail to provide the precision needed to discern the weak diffraction from ML-thick epitaxial layers. Initially, a feasibility and sensitivity analysis was performed to evaluate the potential of the XRD technique.

In order to present the most useful information, some of the more obvious changes on the X-ray rocking curve are omitted,[22] with respect to the LM-InGaAs material situated within ±150 arcseconds near the Bragg peak, resulting in a bright peak highly sensitive to hundredth variations percentage in the LM-InGaAs mole fraction. Free software,[23] tutorials,[24] books,[25,26] and review papers[27–31] on crystal diffractometry are widely available for this purpose. In many cases, around the Bragg condition $CuK_{\alpha 2}$ radiation causes additional peaks and fringes to appear; therefore, beam conditioning is highly recommended.

The RTD structure has limited periodicity. Instead, there are groups of similar lattice constants sandwiched between others, which lead to the diffraction to cause a pronounced effect analogous to an optical interferometer with a variation in the incident angle ω. Therefore, unlike a highly-periodic structure, RTDs typically exhibit lower magnitude repetitive group of "satellite" fringes. Very limited information on XRD performed on mesoscopic RTDs is available. The only study known to the authors contains a very high-resolution rocking curve, which was confirmed with destructive HAADF-TEM analysis.[32] Unfortunately, such sensitivity is not always available. Similar XRD rocking curves were reported on other shallow-emitter devices such as InP high electron mobility transistors.[33,34]

Upon preparing the simulation model for XRD, as the doping layers are typically neglected, one would notice a total of 13 layers for the structure presented in Fig. 1. For the purpose of a sensitivity analysis, this is reduced to 6 top (LM-AlInAs layer ignored) or 7 layers, momentarily ignoring the contribution of the buried layers.

Figure 2 shows a modeled comparative structural sensitivity study to ω–2θ X-ray diffraction rocking curves. The vertical axis is a logarithmic scale measure of simulated diffracted particle counts and is plotted from what we consider to be a realistic noise floor for a larger variety of instruments (∼4.5 orders of magnitude from substrate peak). The curves are offset for clarity. No quantization or white noise is added to this analysis. The arrows in the inset indicate the use of layer (parameter) linking, and all commercial XRD fitting software the authors used during this work included this feature. The rationale behind linking structural parameter changes to similar layers lies with the expectancy of identical growth conditions (including growth rate, temperature, gas intermix ratio, etc.); therefore, on a first-order approximation, a slight change in one layer is likely to affect the other. Should there be manual intervention during growth based on *in situ* characterization data (i.e., given by pyroreflectometry, RHEED, etc.), we always recommend layer linking as a starting point to fit the modeled structure to measurements.

Figure 2(a) presents this idealized model and variations of ±10% thickness of the $In_{0.8}Ga_{0.2}As$ layers. The linkage means that for a −10% thickness variation of the top layer (7.2 nm), the QW is

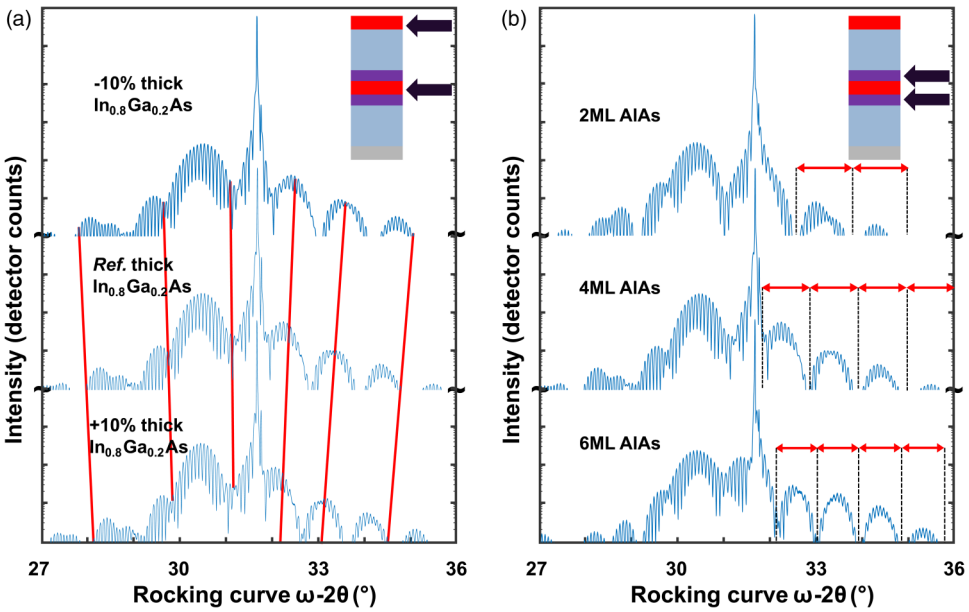

FIG. 2. (a) Symmetric [004] X-ray diffractometry rocking curve with incident (ω) and diffracted (θ) angles, presenting synchronous variations in the (a) $In_{0.80}Ga_{0.20}As$ (b) and AlAs layers thickness. Vertical scales are logarithmic. The inset is a simplified representation of Fig. 1. Red lines connecting the satellite valleys are a guide for the eye. Modeled curves presented without the intentional addition of noise.

expected at 3.43 nm. These values are arbitrarily chosen to help guide the eye. In practice, such a large value drift would cause a change in the performance of an RTD,[7] possibly leading to catastrophic failure due to hot carrier effects. From this figure, two overall trends are apparent: by following the red guidelines, the shape of the highly-strained $In_{0.8}Ga_{0.2}As$ peak is "compressed" between a narrower range of the rocking angle and drifts further apart, as expected, from the InP peak. These red guidelines are excellent markers to visualize the DBRTS strain regimen, which is why we recommend manual fitting in the first instance in this complicated, low-signal case, over a machine residual-based fit algorithm, which may neglect this peculiarity. Because the system is partially strain-balanced, this attracts an even more noteworthy shift toward the Bragg peak of the AlAs satellite layers. The periodicity of the satellites is shortened with increased thickness, but this effect is comparably smaller to the one presented in Fig. 2(b), where the exact opposite behavior is apparent. Symmetrically increasing the AlAs thickness greatly alters the periodicity of the satellite peaks (expressed with the approximately equidistant red arrows), whereas the highly-strained InGaAs regimen sees negligible changes (noticeable with a change in symmetry at the bottom of the "Pendellösung" fringes). These are also fine markers that an "autofit" processor may neglect. It is, therefore, that with this modeled contribution, and knowing the overall trend, it is possible to ascertain the sensitivity to relatively minor epitaxial changes.

These minor differences make it such that equipment with adequate sensitivity (~5.5 orders of magnitude of count intensity from the InP peak recommended) can effectively characterize RTDs via fitting. Though there is overlap, it is possible to deconvolute the contribution of the two, given that a sufficient signal to noise ratio (particularly above quantization noise) is obtained. With this in mind, most HR-XRD systems are expected to be capable of characterizing pseudomorphically grown AlAs/InGaAs/AlAs RTDs, in the worst case, to AlAs to ±2 ML, QW width to ±2 ML, and $In_xGa_{1-x}As$ mole fraction to ±7%. With careful fitting, longer integration time per data point, and therefore good signal-to-noise ratio, the characterized precision of the barrier thickness is ±1 ML (shown in Table I, column 1) based on the sensitivity of the simulation to structural inputs to provide quantifiable changes to the satellite fringes in Fig. 2(b), and Pendellösung spacing of Fig. 2(a). Assumptions include that the lattice parameter constants are known to at least 4 decimal points (0.586 97 nm at 300 K for InP); therefore, the Bragg angle can be precisely computed, assuming that Vegard's law applies for InGaAs mole fractions. Beam symmetry and secondary contributions are neglected for this sensitivity analysis. No wafer curvature is assumed. E_1 sensitivity is determined by additional mesoscopic transport modeling based on these structural input sensitivities, assuming valence band offsets of 718.6 meV for $In_{.53}Ga_{.47}As$ on AlAs and 834.6 meV for $In_{.80}Ga_{.20}As$ on AlAs, computed using the model solid theory[35] with additional parameters from Refs. 36 and 37. It is important to note that a regular square well potential solver is insufficient to calculate E_1 with precision, as the wavepacket wavefunctions in the DBRTS interact and merge, changing the overall bound levels. A computational approach based on Green's functions was employed, assuming a

TABLE I. Error of characterizing the double barrier-QW system including well width (t_w) and $In_xGa_{1-x}As$ mole fraction (as [In %]), barrier thickness t_B, and the corresponding shift in 1st electron quasibound energy (E_1). The bold face highlights the advantage of each technique.

	HR-XRD	HR-XRD w/C-well	LT-PL w/C-well	HR-XRD and LT-PL w/C-well
AlAs t_B (ML)	±1	**±0.5**	±1	±0.5
QW t_w (ML)	±2	±1	±1	±0.5
QW [In] (%)	±7	±4	**±2**	±2
E_1 (meV)	±20	±15	±12	±5

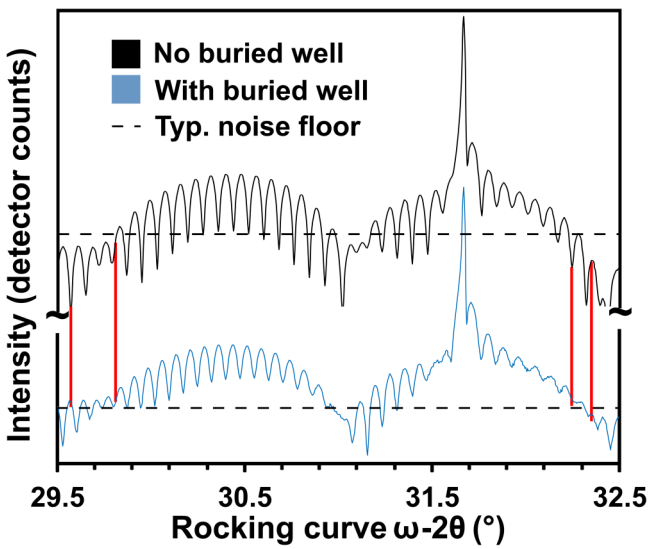

FIG. 3. Comparison of modeled symmetric [004] XRD rocking curves with (bottom) and without (top) the active region copy (C-well). Typical noise floor for this measurement is shown with a dotted line. Red lines as a guide for the eye.

virtually zero scattering parameter for the sensitivity analysis, to avoid increasing the E_1 linewidth. The electron transport modeling is the subject of our previous work.[7]

B. Inclusion of a buried active region copy

The inclusion of a buried copy of the active region (C-well), shown in the lower part of Fig. 1, was mentioned in our previous work.[38] In Fig. 3, we show the modeled contributions of the buried well to the [004] symmetric XRD rocking curve. The immediate benefit is a +3 dB increase in overall peak signal magnitude for the AlAs and strained areas, noticeably bringing some of the higher misfit strain regions above the expected noise floor for many systems. Even if this area is viewable, we remind the reader that measurement data often contain quantization noise, which is in the first order of magnitude and is difficult to appreciably remove. The caveat is that the differential magnitude of the Pendellösung fringes is significantly lowered, though not to an extent which could prevent accurate fitting. Overall, the effect could be described as beneficial with respect to the precision of fit predictions.

Figure 4 presents a comparison of the XRD rocking curve on structure B. The attached table presents color-coded information in the style of the layers in Fig. 1. The staircase-doped emitter and collector layers were grouped in one layer; though for the purpose of maximizing the fit accuracy, it is possible to keep them separated. Degenerate doping has been known to increase the lattice stress[39] and, therefore, roughen the surface morphology.

The fit shows good agreement with the strained InGaAs layers. This suggests a high quality of the QW region in the scanned area. On the other hand, the peak to valley ratio of the AlAs satellites is noticeably lower in the measurement. As the height difference for a 100 μm^2 spot size due to the worst-case offcut is 250.05 pm, therefore <1 ML, and the wafer itself did not have any measurable bow due to accumulated stress, we may conclude that this reduction is due to local fluctuations of the AlAs/InGaAs interface.

At the Bragg peak, the AlInAs could be easily deconvoluted from other LM-InGaAs sources, due to it being a single, bulk layer with a known target thickness. It was found that the indium mole fraction was +2.34% off from the target x = 0.52 LM condition. Though great computational effort can be spent in exactly

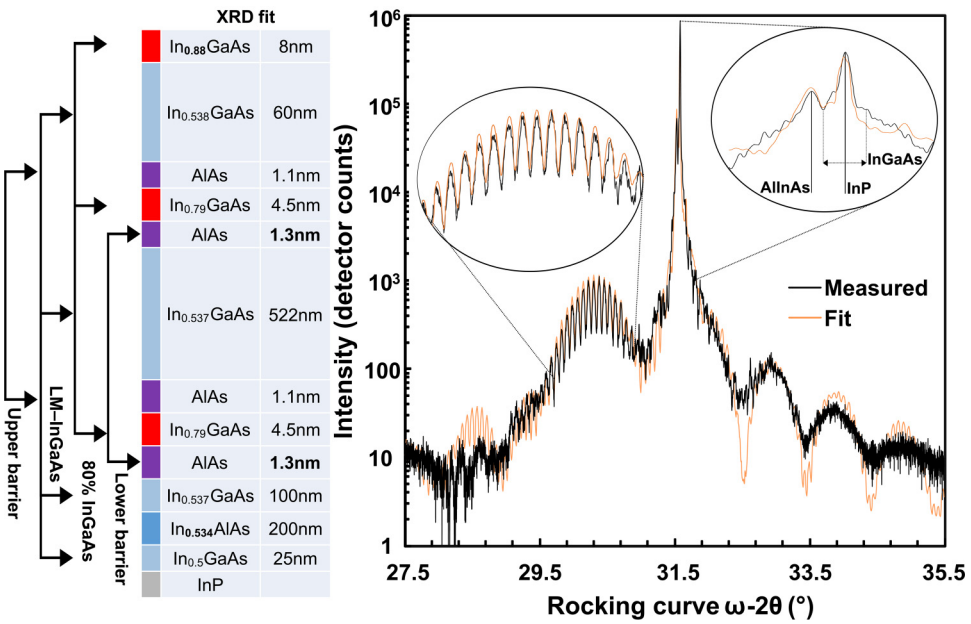

FIG. 4. High-resolution X-ray diffraction rocking curve of structure B (15 ML QW), comparing measurement with the fit. (left) Parameter-linked epitaxial layers to obtain a 1st fit. (table) Result of the fit shown with the color-coded simplified layer structure of Fig. 1, with bold numbers as gross variation from the designed structure. (left inset) Detail of the $In_{0.8}Ga_{0.2}As$ compressive region. (right inset) Detail near the Bragg peak, shown with solved AlInAs and InGaAs layers.

attributing each mole fraction of the LM-InGaAs layers, ultimately, this does not present useful information for the overall characterization scheme and was ignored, instead of using an average value of close fit. The top $In_{0.8}Ga_{0.2}As$ cap was fit with a 34% relaxation and a slightly richer mole fraction of $x = 0.88$, which concurs with observations of occasional X-shaped defects (1–2/field of view) under a Nomarski microscope, and submicrometer surface roughness preventing effective grazing incidence XRD to be performed. The film is above the calculated critical thickness for this molar fraction.[7]

The thickness of the AlAs barriers was left for last, as it is an exercise in finesse. The thickness for all AlAs barriers was initially linked, then the top and bottom barriers of the active region and C-well were separated to achieve a finer fit. Lower resolution XRD may only be able to reliably detect gross variations (see Sec. V). "Nearest neighbor" curve fitting algorithms are generally more suitable than humans at fitting fine features, though to maximize the physical meaning and reduce computational time, we could only recommend this as an optimization step with no more than 3–4 parameters with appropriate lower/upper bounds set.

Lower resolution data for structure A were presented recently.[40] The best fit to this structure has suggested an $In_{0.87}Ga_{0.13}As$ QW and a bottom and top AlAs barrier of 1.3 and 1.1 nm, respectively (both active and dummy regions). The QW width was found to be within the design tolerance at 3.9 nm, and the top cap was also found to be indium-rich $x = 0.87$, and slightly thinner, at 7.8 nm. The inclusion of the C-well, therefore, increases the likelihood of an accurate characterization. Due to an increase of magnitude of the peaks in both the compressive and tensile regions, the AlAs barriers, as now there are 2 pairs, can be determined to ±0.5 ML confidence on samples with high quality interfaces. We remind that an empirical measure of this interface quality is the overall similarity of the peak to valley ratio of the satellite fringes in the obtained data vs the model. On modeling software that has this capability, the peak to valley ratio can also be lessened by wafer curvature (a natural effect of strain relief). The experimental ω–2θ calibration and optimization stages as well as the slit configuration may also influence these low-signal areas.

The QW remains more difficult to deconvolute compared to LT-PL, with the QW width to ±1 ML and depth to ±4% (see Table I, column 2). Based on TEM scans of the structure and MOVPE growth dynamics, we speculate that the inaccuracy regarding the InGaAs mole fraction is due to the nonuniform spread of group (III) atom species throughout the QW. In high-strain situations, indium tends to accumulate in rich pockets. With increasing indium concentration and susceptor temperature, there is a risk of relaxation into 3-dimensional island quantum dot (QD)-like structures, which affects the local uniformity of the thin AlAs barriers. As the QW width is inextricably linked with its depth in terms of accumulated stress, there is some significant uncertainty, only helped by the more precise determination of the AlAs barrier thickness. Overall, the parameter space for determining E_1 can be reduced. If E_1 can, therefore, be determined experimentally (Sec. IV), using mesoscopic transport modeling as a guide (Sec. V), accurate QW characterization can be obtained from the HR-XRD fit (see Table I).

IV. LOW-TEMPERATURE PHOTOLUMINESCENCE SPECTROSCOPY

In the previous work,[21] we have highlighted that PL is a powerful technique for estimation of the n^+ doping level using the Moss-Burstein effect; variation of the doping across the wafer, confirmed with Hall effect measurements, and LT-PL mapping was performed.[40] Equally important, PL showed variations of the LM-InGaAs mole fraction at less than 0.6%, observation sustained with the good fit around the Bragg peak of Fig. 4. At low temperature, we have identified the QW emission from undoped (type-II) and doped (type-I) QWs.[38] There are 3 such transitions expected: the bulk LM-InGaAs bandgap, and transitions arising due to the QW, where type-I and type-II radiative transitions are attributed to the active region, QW surrounded by doped n+ contacts, and unintentionally doped (UD) buried QW, respectively. We have previously confirmed the emission using electrochemical capacitance-voltage (eCV) profiling.[38] We have, therefore, highlighted the need for low-temperature measurements as raising the sample temperature above 50 K results in a broadening and merging of these features.[5]

However, as the excitons are expected with a diameter of 10–20 nm, averaging resulting in spectral overlaps and broadening can occur. This has been extensively reported by Herman *et al.*[41] Power-dependent LT-PL was performed with excitation densities ~0.1 to ~350 W cm^{-2}. Beyond these values, red shift of the bulk InGaAs emission is often observable in our experimental setup. This heating effect suggests an upper bound for our heatsinking capability.

Figure 5 is a representative PL spectrum at a moderately low excitation power of ~0.6 W cm^{-2} on the virgin surface of the wafer. The inset of Fig. 5 shows a schematic representation of the radiative transitions observable on the spectrum. Due to the comparatively larger thickness of material (~1 μm vs <6 nm), the most intense peak of the spectrum is expected to be the bulk LM-InGaAs (measured at 803 meV), whereas 816 meV is attributed to the bandgap of $In_{0.53}Ga_{.468}As$, using the Varshni parameters recommended by Vurgaftman *et al.*[37] The 13 meV difference is attributed to the exciton binding energy[42,43] and is consistent with our previous observations.[21] The FWHM of the InGaAs peak was fit to 5.4 meV at 15 K. Temperature dependent measurements of the sample project an FWHM of 3.35 ± 0.2 meV at 0 K, in line with the ~3.3 meV prediction of $In_{0.53}Ga_{.47}As$ without alloy disorder.[44] This suggests an overall high quality of the lattice-matched layers,[45] observation confirmed by the relative absence of distinguishable peaks in the HR-XRD rocking curve near the Bragg angle.

The type-I emission is broad and consists of a number of features. Figure 5(b), after Herman *et al.*,[41] shows a schematic of realistic AlAs/InGaAs/AlAs interfaces, exhibiting both large steps of a certain QW width and localized roughness due to the mismatching atom species probabilistically attaching in a nonuniform manner due to a transition toward a new lattice constant. The DF-TEM images of Fig. 1 show that this layer of uncertainty does not extend beyond 1 ML in our structures. However, the island growth mode creating 1 ML steps is the cause of the "peak splitting" at low pump power [as seen in Fig. 5(a)]. The effect remains at higher pump power, where the line of best fit to follow the type-I transitions is given by 3 separate Gaussian components. Herman *et al.*[41] described this effect in their work in

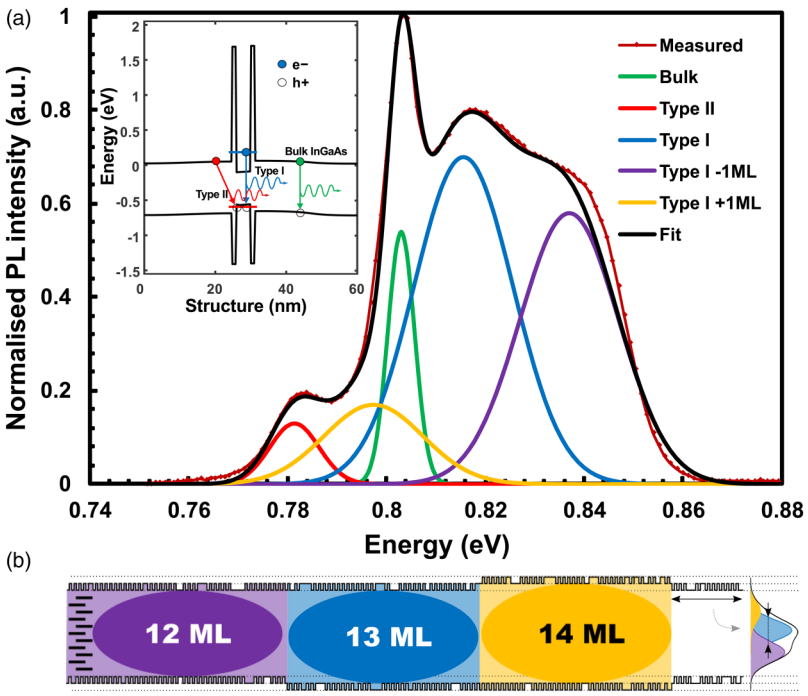

FIG. 5. (a) Representative LT-PL spectrum (dark red line with data points) of the RTD structure on the virgin grown surface. Continuous black line is a best fit realized from the addition of several Gaussian profiles attributed to bulk InGaAs (green) type-II emission (bright red) and type-I QW emission, fit to 3 different well widths in atomic monolayers. (inset) Visualization of the n+ band potential, with 0 set as the Fermi level, schematically showing the type-I, type-II, with the same color scheme. (b) Schematic representation, approximately to scale, of the AlAs/InGaAs QW interfaces, showing large islands of well widths in monolayers and localized roughness. The former yields different excitonic wavelengths, whereas the latter is expected to broaden the full width to half-maximum of each peak.

Figs. 8(b) and 8(c). Figure 5(b) shows a combination of coexisting stepped and rough AlAs/InGaAs interfaces, causing the peak splitting as well as the broadening, respectively. The fit for all type-I emissions is plotted in Fig. 5(a), where we find a FWHM linewidth of 20 meV, and the 3 components are split another ~20 meV apart, at 796, 816, and 837 meV. The low-magnitude peak at 796 meV was added after no satisfactory fit could be attained with only 2 type-I contributors. With the type-I emission, the line of best fit was found when a 3rd emission peak is added at 796 meV. In order to make best physical interpretation of the results, the FWHM was kept constant within all type-I emissions. The ratio between the peak emission intensity of the type-I/type-I −1ML/type-I +1ML is 1/0.83/0.24, suggesting an average QW width between 3.7 ± 0.2 nm, slightly shorter cf. design (3.81 nm). Our previous work[38] has not identified these 3 peaks. The precision of the LT-PL technique aided by the C-well is summarized in Table I, column 3. By pairing the experimental LT-PL with mesoscopic transport modeling on a range of structures, the effects of each parameter are explored. E_1 is deduced directly, with errors given by the experimental apparatus and spread of the data (seen in Fig. 6). Additional samples show greater variance, leading to the deduced ±12 meV possible variance in E_1.

However, the type-I transition energies alone do not provide sufficient information to determine E_1, as the valence band offsets of the AlAs/InGaAs heterointerface depend on local strain vectors.[46] Type-I transitions sample both confined hole and electron states. The type-II emission, in contrast, chiefly samples the QW hole states. Multiple QW thicknesses yield a separation of ~¼th of the type-I emission according to our modeling. Therefore,

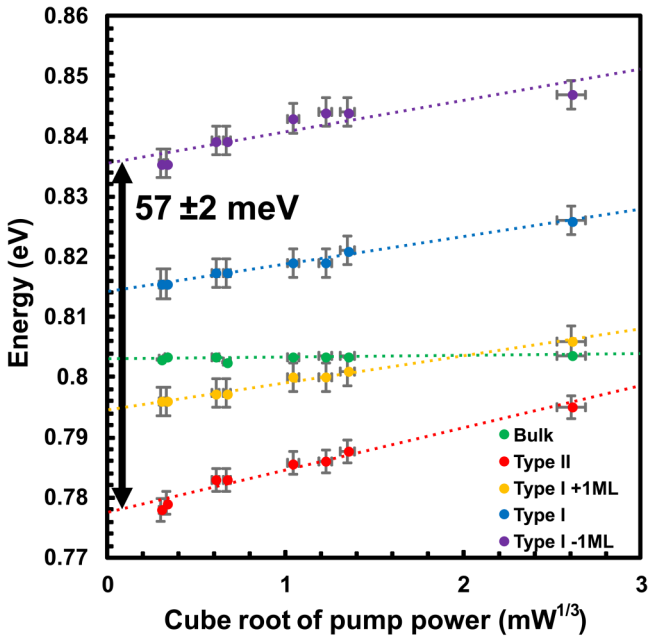

FIG. 6. Power-dependent spectral peak shifts using the color coding of Fig. 5. The dotted lines serve as an extrapolation toward the limit of no pump power. The markers are error bars, with the horizontal crosshair representing the worst-case pump power instability over time (±3%), and the horizontal bar as a median error of the measurement system (~ ± 2 meV).

in Fig. 5(a), only one Gaussian is used to fit the type-II emission, despite the usage of signal recovery techniques to increase the apparent noise floor of the system.

V. ANALYSIS AND STRUCTURAL ASSESSMENT

Combining the HR-XRD and LT-PL techniques offers better confidence in the structural description than either of them in isolation. The key to this effort is to obtain AlAs barrier thickness from the HR-XRD (with C-well) fit with the greatest precision available. As LT-PL provides detailed compositional information about the QW, as well as the preponderance ratio of different QW widths, it is now possible to solve the QW width with enhanced precision, consequently, leading to less error of determining E_1.

In order to confirm the effect of the structural roughness, PL the pump power was varied, and the type-I emission peaks were extracted via curve fitting and presented in Fig. 6. The confined energy of type-II transitions is shown to vary with the cubic root of the excitation power by Ledentsov *et al.*[47] and is similarly depicted in the canon.[48,49] Newer understanding suggests a split between a ½ and ¼ power dependency of the type-II transitions,[50] with the canonical graphical representation remaining an adequate approximation. Firstly, we note that in the excitation power-dependent PL spectra the bulk LM-InGaAs peak does not shift outside of the measurement error (< ± 2 meV) with pump power, suggesting that the "thermal bonding" of the sample "is adequate." Secondly, plotting all fitted type-I transitions from the QW widths, from the target width and ±1 ML, we note that the slope of the shift with pump power (and, therefore, sample heating) is consistent. Furthered with the maintenance of the FWHM against all 3 type-I transitions for the same pump power, we consider that this is a good qualitative and quantitative portrayal of the InGaAs/AlAs interfaces' roughness. Previously, we have also performed a LT-PL line-scan along the (001) crystal surface, with a cleaved section of the RTD material placed with the (110) crystal surface perpendicular to the incident laser beam.[38] Moreover, the type-II transition appeared to be more sensitive to increased carrier density, a trend observed with all similar RTD materials we have studied in the past and is attributed to the collected charge forming a triangular well in the emitter/collector regions.

The line fit intercept with the vertical axis shows the value of a given emission in the limit of zero pump power, or, in other words, the theoretical absence of the excitation of laser light. Figure 6 displays this limit, and the difference between the maximum type-I emission and type-II emission represents the upper energy level of the weakly bound E_1 level inside of the conduction band QW. We remind the previously modeled[7] contribution of the E_1 state on the device operating characteristics; therefore, it is important to know this parameter. The heavy hole weakly bound emission (Hh_1) was computed at 4 meV; therefore, it is practically merged with the valence band potential edge.

In addition to the 13 meV binding energy of carbon impurities in the LM-InGaAs, we use a binding energy of 7 meV consistent with practical studies of InGaAs type-I QW.[51–53] We assume a binding energy of 1 meV based upon type-II examples in thin GaSb/GaAs QW.[47] Therefore, the new type-I emissions are computed at 844/821/803 nm for the 12/13/14 ML QW widths, respectively.

In order to better correlate the findings of Fig. 6 in the context of the DBRTS structure, such as varying QW widths and ternary alloy mole fraction (i.e., QW depth), we explore this space using a previously established modeling methodology[7] and plot the shift in transition energies. Figure 7(a) does so for the type-I and Fig. 7(b) for the type-II emission. Both the emissions have a monotonic decrease in energy level with an increase in QW width and QW depth (i.e., InGaAs mole fraction increases). The emission can also shift with AlAs barrier thickness, computed as a −12 nm shift for symmetric barriers of −1 ML thin and +5 nm shift for symmetric barriers +1 ML thick (vs the 4 ML target structure). Practical average barrier thickness deviations from these ideal thicknesses are expected to produce intermediary values and further broadened FWHM of the Gaussian types, as the interface roughness increases.

Considering either type-I or type-II transitions in isolation does not provide a unique solution for the well width and depth. The two energy lines in the limit of no pump power extrapolated from power-dependent LT-PL can be correlated with the plots

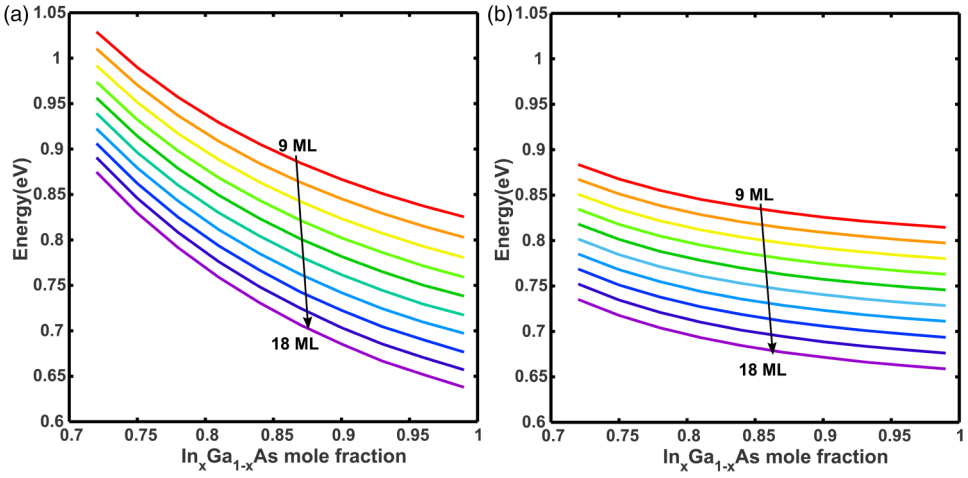

FIG. 7. Computed transition energies of the type-I (a) and type-II (b) emission, with varying InGaAs mole fraction and QW widths. Each curve represents a QW width step of 1 atomic monolayer.

of Fig. 7, though their intersection typically provides a range of 7–9 different combinations of QW widths and depths, if a ±1 ML variation in AlAs is assumed. However, the difference between the two equates to an experimental determination of E_1. This additional parameter allows fine-fitting of the simulation results, as bandgap energy[46] and valence band offsets[35] are known to vary depending on the structural strain vectors. Inclusion of the C-well is, therefore, critical in allowing both parameters to be simultaneously obtained. Figure 8 plots all possible solutions that give the experimentally determined type-I emissions (expected to correspond to QWs of 12, 13, and 14 ML) and type-II emissions (13 ML), for PL peaks in the limit of zero pump power and corrected for excitonic binding energies. Type-II ±1 ML is not plotted, as the 3 components could not be clearly resolved experimentally. This happens in part due to the expected spacing of 10–12 meV, and the type-II emission being situated close to the detectivity limit, particularly problematic at low pump powers where the peak splitting is expected to occur. Cryostat temperatures lower than 12 K were also not available during this work. If both LT-PL and HR-XRD agree on the AlAs thickness, it is considered unnecessary to plot the changes brought by AlAs variation in Fig. 8. The intersection point for the as-designed 13 ML QW emission is found at $In_{0.87}Ga_{0.13}As$.

The HR-XRD data of structure A[40] suggested $In_{0.87}Ga_{0.13}As$ with a 13 ML QW and asymmetric AlAs barriers, with top and bottom barriers at 1.1 (as-designed) and 1.3 nm, respectively. It

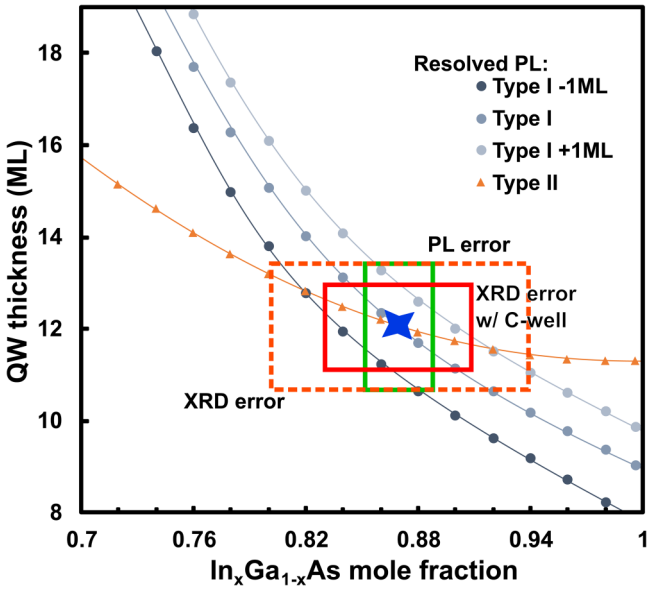

FIG. 8. Resolved PL energies for the zero excitation transition energies of Fig. 5, corrected for excitonic binding energy. Intersection points of the type-I and type-II transition provide possible solutions to the RTD structure (see the text). Points reflect the 2% mole fraction error attributable to the system, as a guide for the eye. The rectangles indicate the error of the three methods in isolation presented in Table I, without consideration to AlAs fluctuations. The convergence of the type-I, type-II emissions, and HR-XRD results in an accurate description of the structure (blue star).

should be noted that a different X-ray system was used for structure B for the data presented in Fig. 4.

The comparison of the techniques is presented in Table I. We note that the quality of the analysis of HR-XRD is highly dependent on instrument detectivity, as well as the pseudomorphic strain condition of the sample, where any relaxation results in increased signal-to-noise ratio and diffusion of the satellite peaks, particularly with respect to the AlAs barriers. Should the AlAs/InGaAs satellite peaks be overcome by quantization noise, the result is a marginal fit. Wide angle range, high integration time rocking curves, performed on a structure with the included C-well is likely to allow a higher quality fit, at the expense of lessening the amplitude of the smaller Pendellösung fringes. In turn, a poor fit due to noisy data lowers the confidence of the obtained structure, which in turn increases the imprecision of the E_1 search space. In order to alleviate this problem, structural parameters are then input to the suitable mesoscopic transport modeling based on PL data, adjusting the strain-dependent valence band offsets as a fit factor, found with 4% and 9% for lattice-matched and DBRTS-strained InGaAs, respectively.[7,46]

Resolving the convoluted PL transitions requires a very careful analysis of the data. Individually, either technique provides a low confidence in the results: LT-PL is less sensitive to minor AlAs barrier variations, whereas HR-XRD was found to be less sensitive to fluctuations of the InGaAs QW mole fraction, with either techniques overall providing an uncertain solution regarding the QW width. Consequently, local nonuniformities could manifest themselves as transitions toward 3D island growths (i.e., increased risk of formation of InAs quantum dots). Due to the different physical mechanisms that allow each technique to function, as expected, LT-PL and HR-XRD are found to be complementary characterization techniques, effective in describing the RTD structure with higher precision than either technique in isolation. This result is summarized in Table I, column 4.

VI. CONCLUSION

We have presented a nondestructive characterization scheme for high current density RTDs capable of describing the atomically thin AlAs barriers, via incorporation of a buried copy of the active region (C-Well). Using a combination of LT-PL to determine the relative energy level of the weakly-confined states and HR-XRD for advanced structural information, whose solutions are cross-referenced with advanced device modeling of the double-barrier-QW structure, a better structural determination can be obtained than either HR-XRD or LT-PL in isolation.

LT-PL confirmed high quality ternary $In_{0.532}Ga_{0.468}As$ alloy lattice matched to InP, by determination of the 5.4 meV linewidth at 15 K, extrapolated toward 3.3 meV in the 0 K limit. This finding is also confirmed by the lack of multiple high-intensity InGaAs peaks near the Bragg angle. The LT-PL spectrum is analyzed against model predictions of optical transitions with a variation in QW width and depth. This has allowed determination of the stability of the indium concentration throughout the QW and the precise QW thickness at the sampled point. In turn, the information from the solved PL spectra is fed back into the fitting of the HR-XRD curve. The degree of the fit to the AlAs satellite fringes is

a gauge of the quality of the AlAs barrier quality and symmetry. This method, therefore, allows fine determination of the structure and conduction band potentials of challenging high current density RTDs and similar n-doped, thin, single QW structures.

ACKNOWLEDGMENTS

This work was supported by the Engineering and Physical Sciences Research Council DTA studentship (No. EP/L505055/1). We are thankful for the technical staff of the James Watt Nanofabrication Centre. R.B. would like to acknowledge the fruitful discussions and help of Dr. David T. D. Childs and Dr. Matthew Steer of the School of Engineering (UoG) for help with using the photoluminescence and HR-XRD kits, respectively, and Dr. Neil D. Gerrard for advice regarding MOVPE reactor specifics, as well as Professor Asen Asenov and Dr. Vihar Georgiev of the Modelling Group (UoG) for providing input on RTD modeling.

REFERENCES

[1]L. Esaki and R. Tsu, IBM J. Res. Dev. **14**, 61 (1970).
[2]R. Izumi, S. Suzuki, and M. Asada, in *2017 42nd International Conference on Infrared, Millimeter, and Terahertz Waves* (IEEE, 2017), pp. 1–2.
[3]S. Kitagawa, K. Ogino, S. Suzuki, and M. Asada, Jpn. J. Appl. Phys. **56**, 040301 (2017).
[4]N. Shimizu, T. Waho, and T. Ishibashi, Jpn. J. Appl. Phys. **36**, L330 (1997).
[5]K. J. P. Jacobs, "Development of resonant tunnelling diode terahertz emitter," Ph.D. thesis (Department of Electronic and Electrical Engineering, The University of Sheffield, 2015).
[6]F. Capasso, K. Mohammed, and A. Cho, IEEE J. Quantum Electron. **22**, 1853 (1986).
[7]R. Baba, B. J. Stevens, T. Mukai, and R. A. Hogg, IEEE J. Quantum Electron. **54**, 1 (2018).
[8]S. Diebold, K. Nishio, Y. Nishida, J.-Y. Kim, K. Tsuruda, T. Mukai, M. Fujita, and T. Nagatsuma, Electron. Lett. **52**, 1999 (2016).
[9]S. Kitagawa, M. Mizuno, S. Saito, K. Ogino, S. Suzuki, and M. Asada, Jpn. J. Appl. Phys. **56**, 058002 (2017).
[10]R. Bernardo-Gavito, I. E. Bagci, J. Roberts, J. Sexton, B. Astbury, H. Shokeir, T. McGrath, Y. J. Noori, C. S. Woodhead, M. Missous, U. Roedig, and R. J. Young, Sci. Rep. **7**, 17879 (2017).
[11]T. Akeyoshi, H. Matsuzaki, T. Itoh, T. Waho, J. Osaka, and M. Yamamoto, in *Conference Proceedings. Eleventh International Conference on Indium Phosphide and Related Materials (Cat. No. 99CH36362)* (IEEE, 1999), pp. 405–410.
[12]M. Koch, in *Terahertz Frequency Detection and Identification of Materials and Objects SE–18*, edited by R. Miles, X.-C. Zhang, H. Eisele, and A. Krotkus (Springer, Dordrecht, 2007), pp. 325–338.
[13]N. Shimizu, H.-J. Song, Y. Kado, T. Furuta, A. Wakatsuki, and Y. Muramoto, NTT Tech. Rev. **7**, 1 (2009); available at https://www.ntt-review.jp/archive/ntttechnical.php?contents=ntr200903sf7.html
[14]A. Cosentino, Technologies **4**, 6 (2016).
[15]T. de Graauw, F. P. Helmich, T. G. Phillips, J. Stutzki, E. Caux, N. D. Whyborn, P. Dieleman, P. R. Roelfsema *et al.*, Astron. Astrophys. **518**, L6 (2010).
[16]G. García-Calderón, in *Physics of Low-Dimensional Semiconductor Structures*, edited by P. Butcher, N. H. March, and M. P. Tosi (Plenum Press, New York, 1993), pp. 267–297.
[17]K. J. P. Jacobs, B. J. Stevens, O. Wada, T. Mukai, D. Ohnishi, and R. A. Hogg, IEEE Electron. Device Lett. **36**, 1295 (2015).
[18]K. J. P. Jacobs, B. J. Stevens, R. Baba, O. Wada, T. Mukai, and R. A. Hogg, AIP Adv. **7**, 105316 (2017).
[19]P. Roblin, R. C. Potter, and A. Fathimulla, J. Appl. Phys. **79**, 2502 (1996).
[20]R. Beanland, Ultramicroscopy **102**, 115 (2005).
[21]K. J. P. Jacobs, B. J. Stevens, T. Mukai, D. Ohnishi, and R. A. Hogg, J. Cryst. Growth **418**, 102 (2015).
[22]R. Baba, O. Kojima, K. J. P. Jacobs, B. A. Harrison, B. J. Stevens, T. Mukai, and R. A. Hogg, Proc. SPIE **10929**, 1092909 (2019).
[23]S. A. Stepanov, see http://x-server.gmca.aps.anl.gov/cgi/www_form.exe?template=GID_sl_multilay_simplified.htm&method=post for "Dynamical X-Ray Diffraction from Multilayers," GID_sl Web, 2012 (accessed August 9, 2019).
[24]H. Ress and M. Zimmermann, see https://www.bruker.com/events/webinars/good-diffraction-practice-series.html for "Bruker Good Diffraction Practice Series—Webinar series part IV: High-Resolution X-ray Diffractometry," 2012, pp. 1–79 (accessed August 9, 2019).
[25]U. Pietsch, V. Holý, and T. Baumbach, *High-Resolution X-Ray Scattering* (Springer, New York, NY, 2004).
[26]Y. Waseda, E. Matsubara, and K. Shinoda, *X-Ray Diffraction Crystallography* (Springer, Berlin, 2011).
[27]C. Ryang Wie, Mater. Sci. Eng. R Rep. **13**, 1 (1994).
[28]T. Vreeland, and B. M. Paine, J. Vac. Sci. Technol. A **4**, 3153 (1986).
[29]P. Velling, M. Agethen, W. Prost, and F. J. Tegude, J. Cryst. Growth **221**, 722 (2000).
[30]M. Hanke, D. Grigoriev, M. Schmidbauer, P. Schäfer, R. Köhler, U. W. Pohl, R. L. Sellin, D. Bimberg, N. D. Zakharov, and P. Werner, Physica E **21**, 684 (2004).
[31]Y. C. Chen and P. K. Bhattacharya, J. Appl. Phys. **73**, 7389 (1993).
[32]H. Sugiyama, A. Teranishi, S. Suzuki, and M. Asada, Jpn. J. Appl. Phys. **53**, 031202 (2014).
[33]K. Radhakrishnan, T. H. K. Patrick, P. H. Zhang, H. Q. Zheng, S. F. Yoon, and A. Raman, Microelectron. Eng. **51–52**, 433 (2000).
[34]H. G. Lee, S. G. Kim, D. W. Roh, J. J. Lee, and K. E. Pyun, Mater. Sci. Eng. B **47**, 145 (1997).
[35]C. G. Van De Walle, Phys. Rev. B **39**, 1871 (1989).
[36]S. Adachi, *Properties of Semiconductor Alloys: Group-IV, III-V, and II-VI Semiconductors* (Wiley, Chichester, 2009).
[37]I. Vurgaftman, J. R. Meyer, and L. R. Ram-Mohan, J. Appl. Phys. **89**, 5815 (2001).
[38]K. J. P. Jacobs, R. Baba, B. J. Stevens, T. Mukai, D. Ohnishi, and R. A. Hogg, Proc. SPIE **9758** 97580L (2016).
[39]B. Ściana, M. Badura, W. Dawidowski, K. Bielak, D. Radziewicz, D. Pucicki, A. Szyszka, K. Żelazna, and M. Tłaczała, Opto-Electron. Rev. **24**, 95–102 (2016).
[40]R. Baba, K. J. P. Jacobs, B. J. Stevens, B. A. Harrison, A. P. Watt, T. Mukai, and R. A. Hogg, in *2018 IEEE British and Irish Conference on Optics and Photonics* (IEEE, London, 2018), pp. 1–4.
[41]M. A. Herman, D. Bimberg, and J. Christen, J. Appl. Phys. **70**, R1 (1991).
[42]K.-H. Goetz, D. Bimberg, H. Jürgensen, J. Selders, A. V. Solomonov, G. F. Glinskii, and M. Razeghi, J. Appl. Phys. **54**, 4543 (1983).
[43]T. F. Kuech, G. J. Scilla, and F. Cardone, J. Cryst. Growth **93**, 550 (1988).
[44]J. Singh and K. K. Bajaj, J. Appl. Phys. **57**, 5433 (1985).
[45]G. Landgren, J. Wallin, and S. Pellegrino, J. Electron. Mater. **21**, 105 (1992).
[46]S. C. Jain, M. Willander, and H. Maes, Semicond. Sci. Technol. **11**, 641 (1996).
[47]N. N. Ledentsov, J. Böhrer, M. Beer, F. Heinrichsdorff, M. Grundmann, D. Bimberg, S. V. Ivanov, B. Ya. Meltser, S. V. Shaposhnikov, I. N. Yassievich, N. N. Faleev, P. S. Kop'ev, and Zh. I. Alferov, Phys. Rev. B **52**, 14058 (1995).
[48]K. Suzuki, R. A. Hogg, and Y. Arakawa, J. Appl. Phys. **85**, 8349 (1999).
[49]F. Hatami, M. Grundmann, N. N. Ledentsov, F. Heinrichsdorff, R. Heitz, J. Böhrer, D. Bimberg, S. S. Ruvimov, P. Werner, V. M. Ustinov, P. S. Kop'ev, and Zh. I. Alferov, Phys. Rev. B **57**, 4635 (1998).
[50]M. Jo, M. Sato, S. Miyamura, H. Sasakura, H. Kumano, and I. Suemune, Nanoscale Res. Lett. **7**, 1 (2012).
[51]J.-Y. Marzin, M. N. Charasse, and B. Sermage, Phys. Rev. B **31**, 8298 (1985).
[52]Z. H. Lin, T. Y. Wang, G. B. Stringfellow, and P. C. Taylor, Appl. Phys. Lett. **52**, 1590 (1988).
[53]K. Muraki, S. Fukatsu, Y. Shiraki, and R. Ito, Appl. Phys. Lett. **61**, 557 (1992).